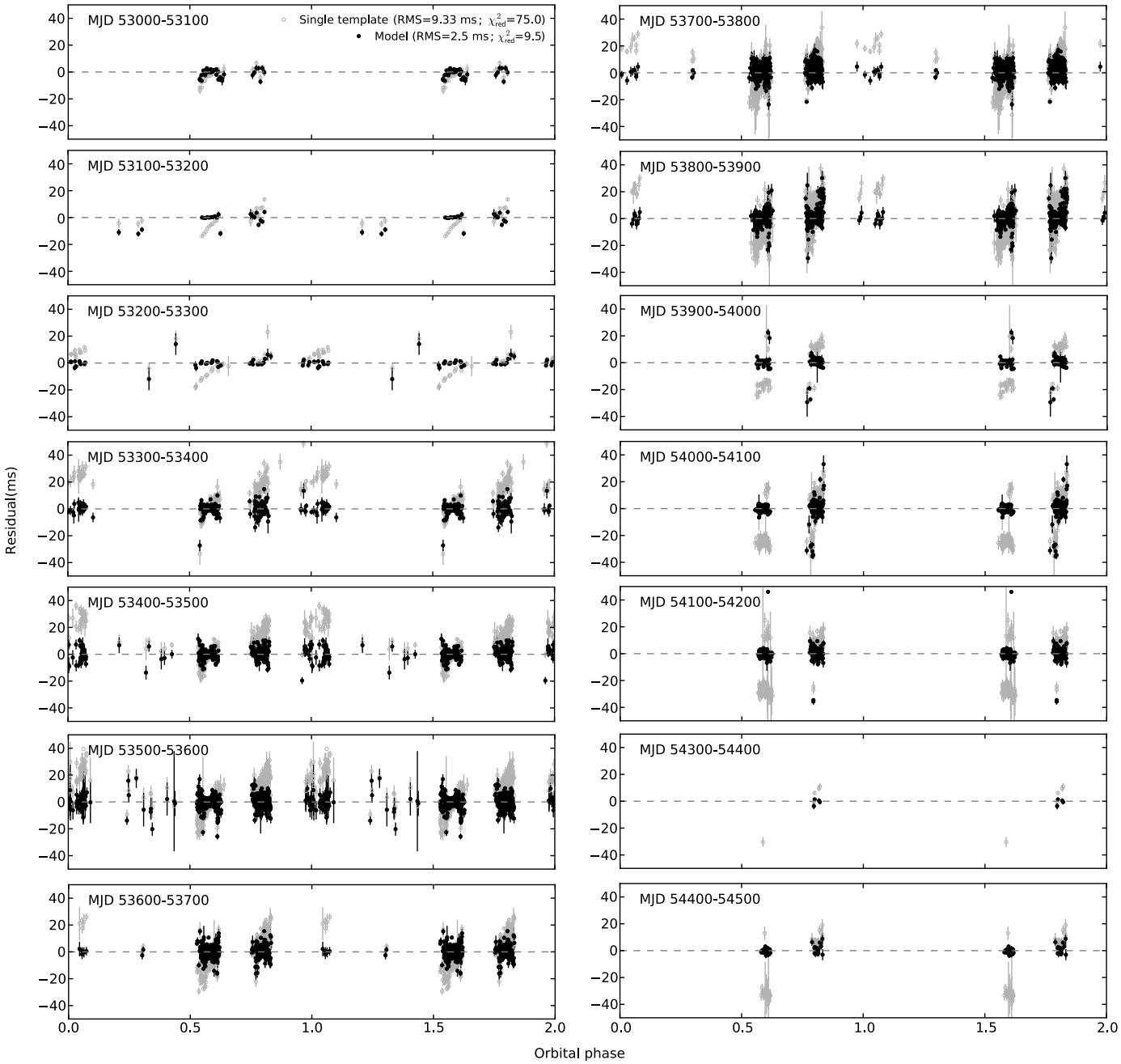

Fig. A.4. (black points) Timing residuals using Gaussian templates of Fig. B.3 and after correcting for the linear drifts across each orbital-phase window, via the best fits shown in Fig. A.2. For comparison, light grey circles show the timing residuals using the fixed WP template profile of Fig. 4. For each data set, the weighted RMS and the corresponding χ^2_{red}, calculated over the entire data set shown in this figure, is shown in the top-right corner of the top-left sub-plot.

Appendix B: Profile evolution

The figures presented in this appendix show the positional and the average profile evolution of the BPs, the IP, and the WP of pulsar B, corresponding to the centroid of each orbital window (the orbital phase at peak brightness), as a function of time, binned in 14 100-day bins. The details of the corresponding analyses can be found in Sects. 3, 4.2, and 4.4.

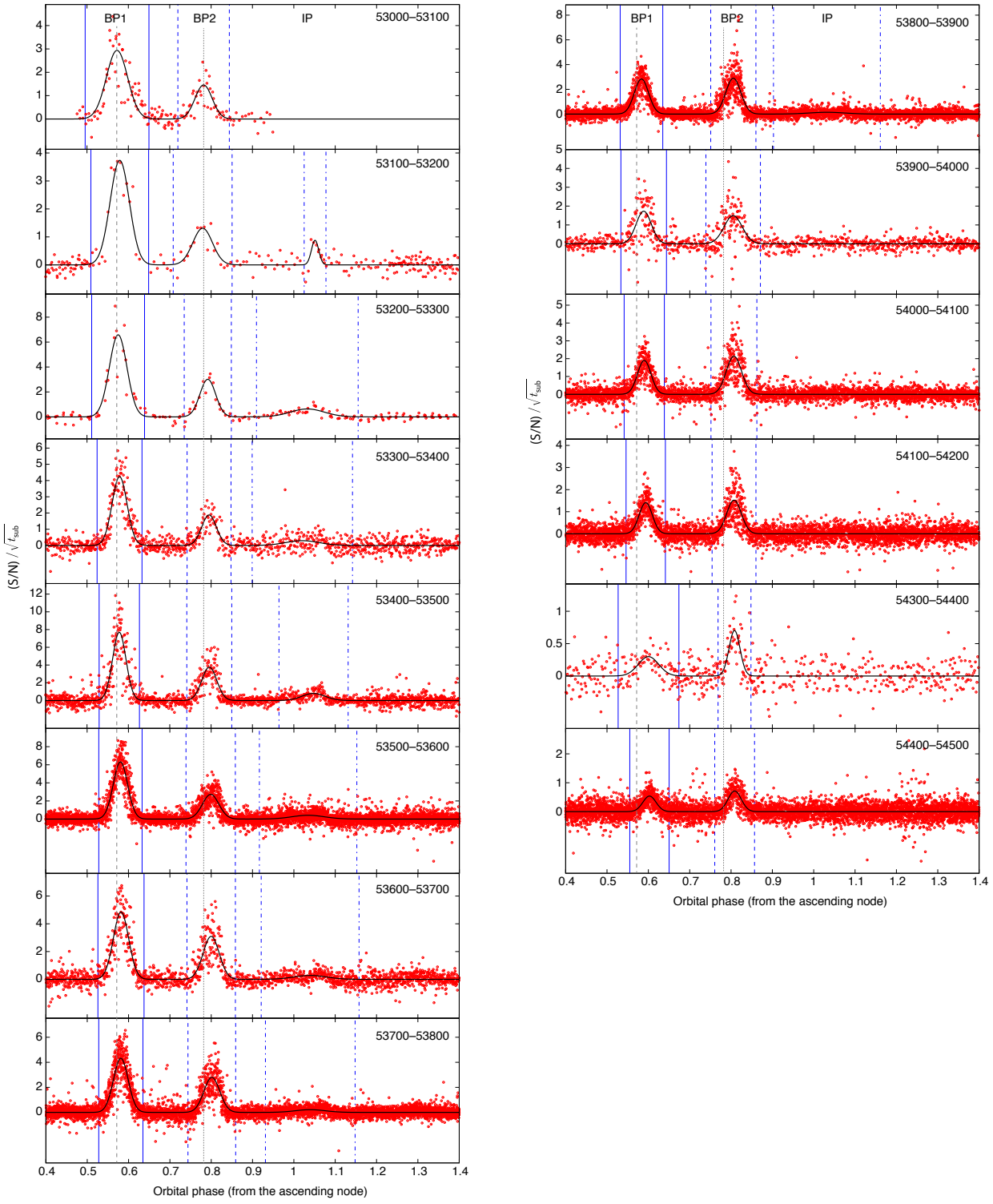

Fig. B.1. Distributions of S/N across the orbit of pulsar B, for each MJD bin (data points). For this figure, the values of the S/N have been normalised by the square root of the integration time. The locations of the two BPs, BP1 and BP2, and where visible that of the IP have been determined using Gaussian fits to the data (black curves). The vertical, solid, dashed and dot–dashed blue lines show the 3σ confidence intervals of the phase locations of BP1, BP2 and the IP, respectively. To emphasise the shift of the locations of BP1 and BP2, as a function of MJD, the dashed and dotted, vertical, grey lines mark the positions of the maxima of the fitted functions for BP1 and BP2, respectively, during MJD 53000–53100.

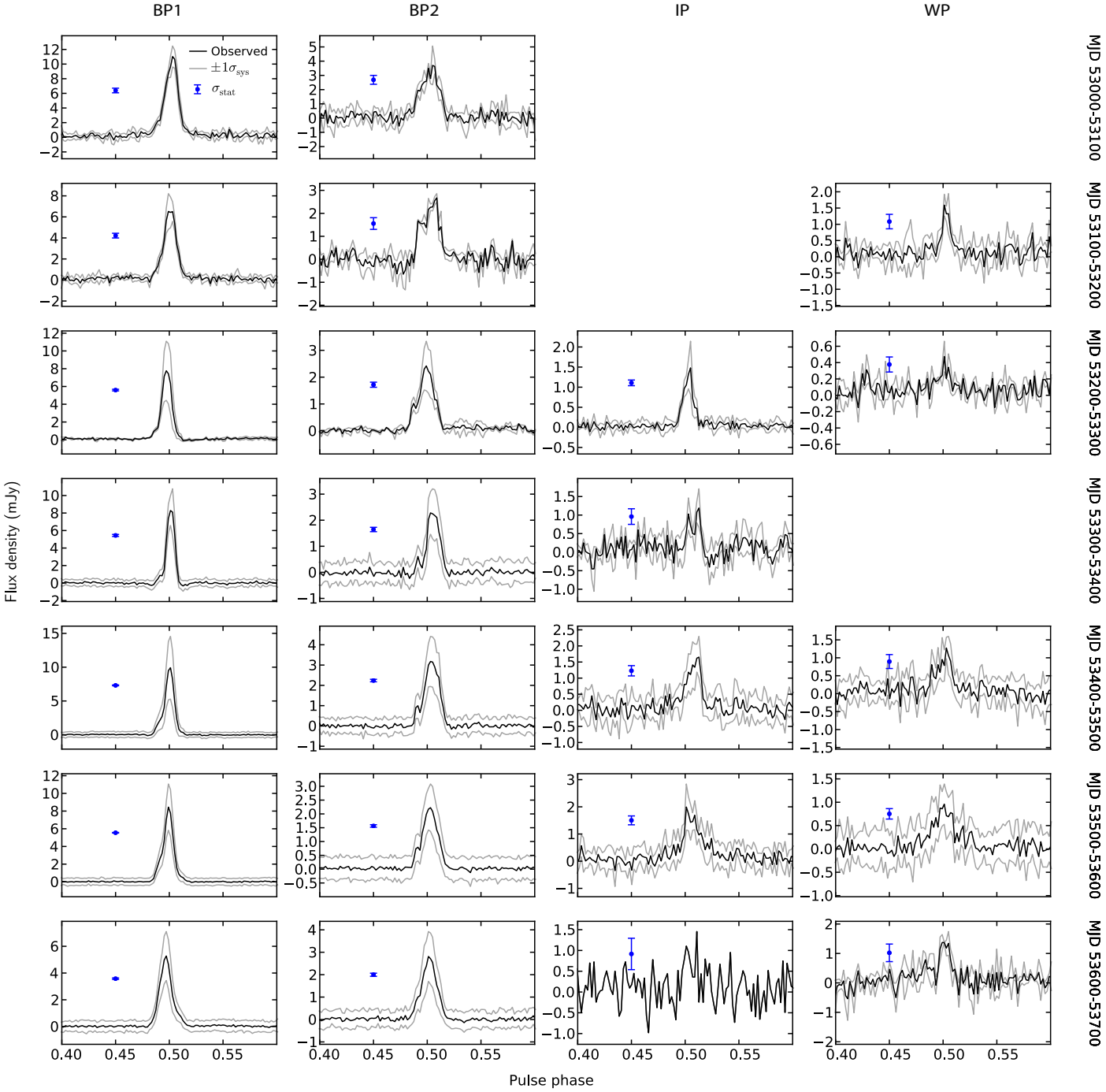

Fig. B.2. Observed average profiles of pulsar B (black lines), corresponding to the centroids of BP1, BP2, and the IP; the WP profiles were calculated using all the data in that orbital-phase window (see blue error bars in Fig. A.1). Each column corresponds to a different orbital-phase window (labelled along the top edge of the figure); each row corresponds to a different MJD bin (labelled along the right edge of the figure). The grey lines show the lower and upper $1\sigma_{\rm sys}$ confidence limits (Eq. (7)). The blue vertical error bar next to each profile corresponds to the off-pulse RMS, $\sigma_{\rm stat}$, of the average profile.

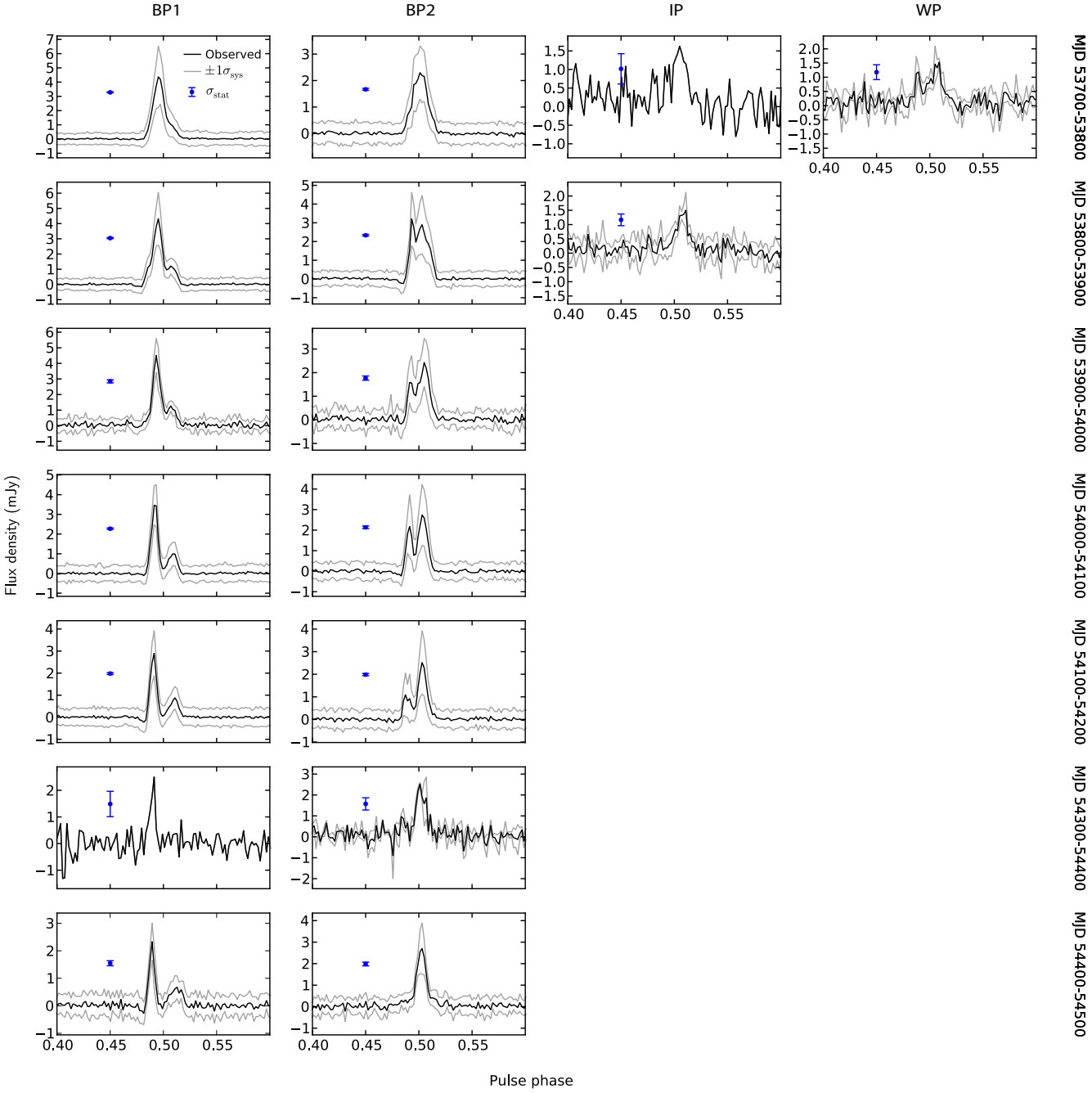

Fig. B.2. continued.

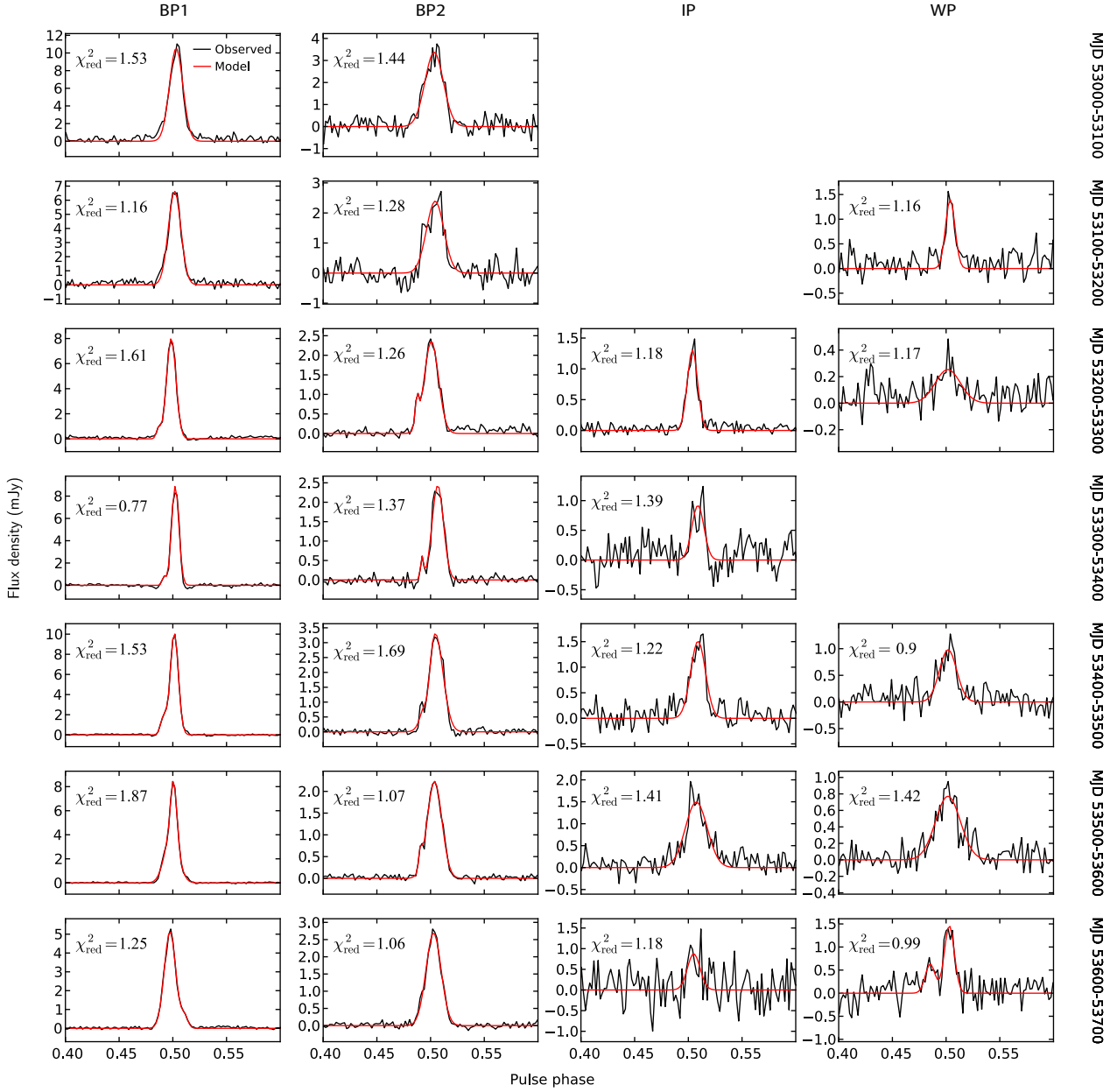

Fig. B.3. Comparison between observed average profiles of pulsar B (black) and the best fit Gaussian templates (red), as described in Sect. 3.2.3. The profiles shown have been tabulated according to orbital-phase window (columns): BP1, BP2, IP, and WP, and the MJD range (rows). The reduced chi-squared value shown for each plot has been calculated using only the off-pulse RMS (σ_{stat}) as weights.

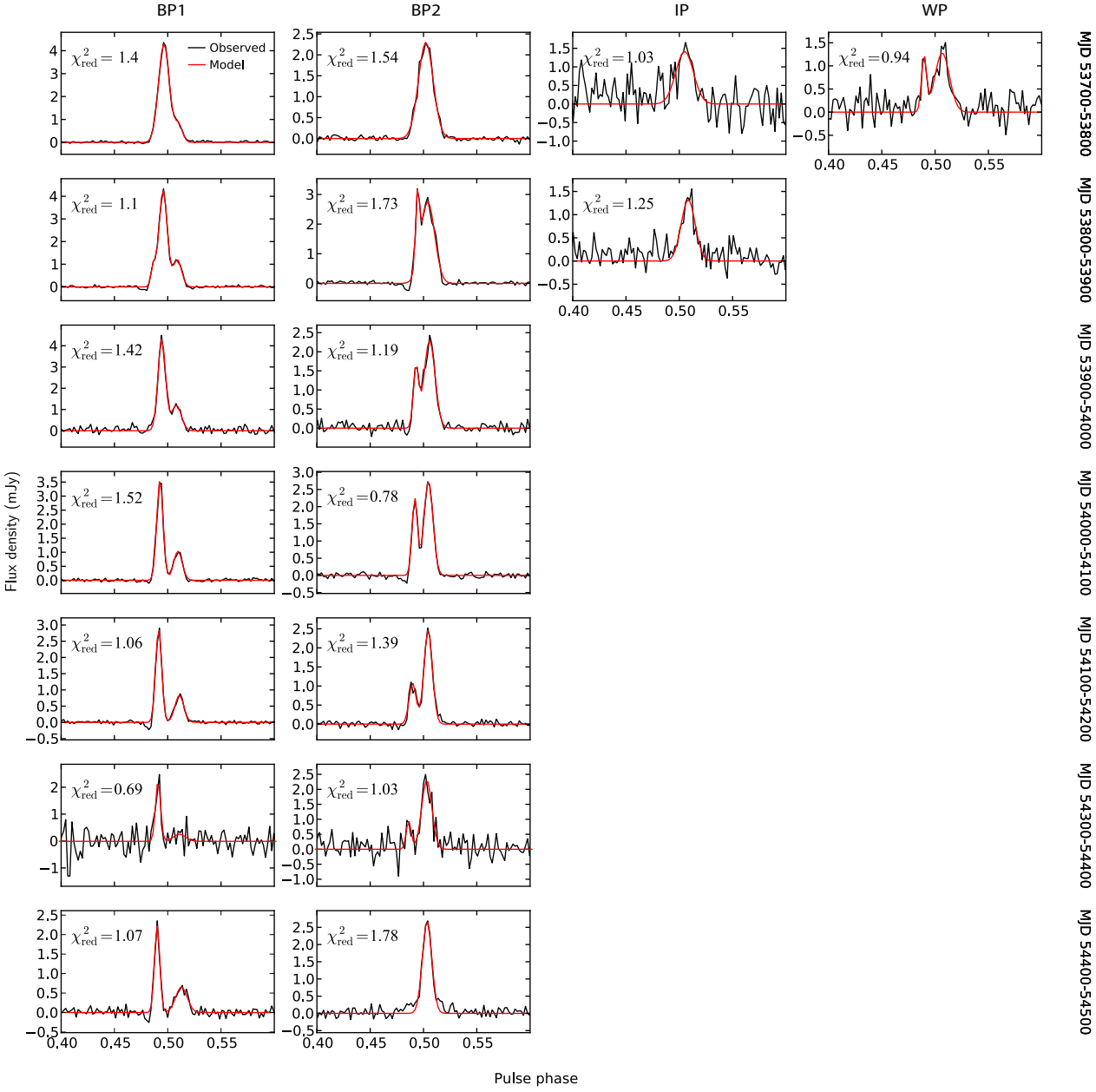

Fig. B.3. continued.

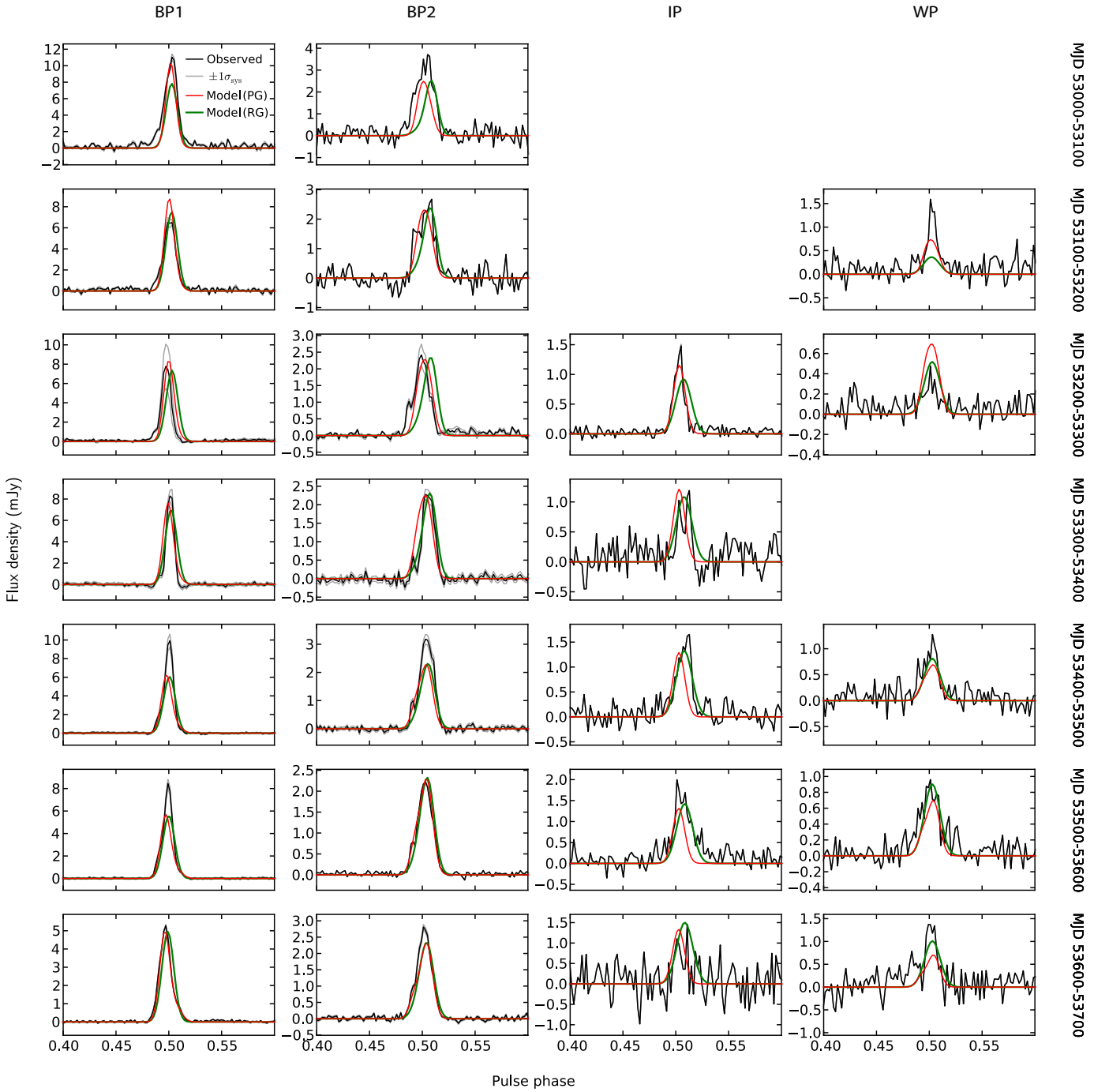

Fig. B.4. Comparison between observed profiles (black) and those produced by our simulation, as described in Sect. 4, using the model parameters with the highest likelihood and a prograde (PG) pulsar spin (red). Green lines show the most likely profiles of an alternative model with a retrograde (RG) pulsar spin. The profiles shown have been tabulated according to orbital phase window, that is, BP1, BP2, IP, and WP, and the MJD range to which they belong. The grey lines show the lower and upper $1\sigma_{\rm sys}$ confidence limits of the observed flux density, multiplied by the most likely error coefficients (q_{kj}) that were derived from our analysis.

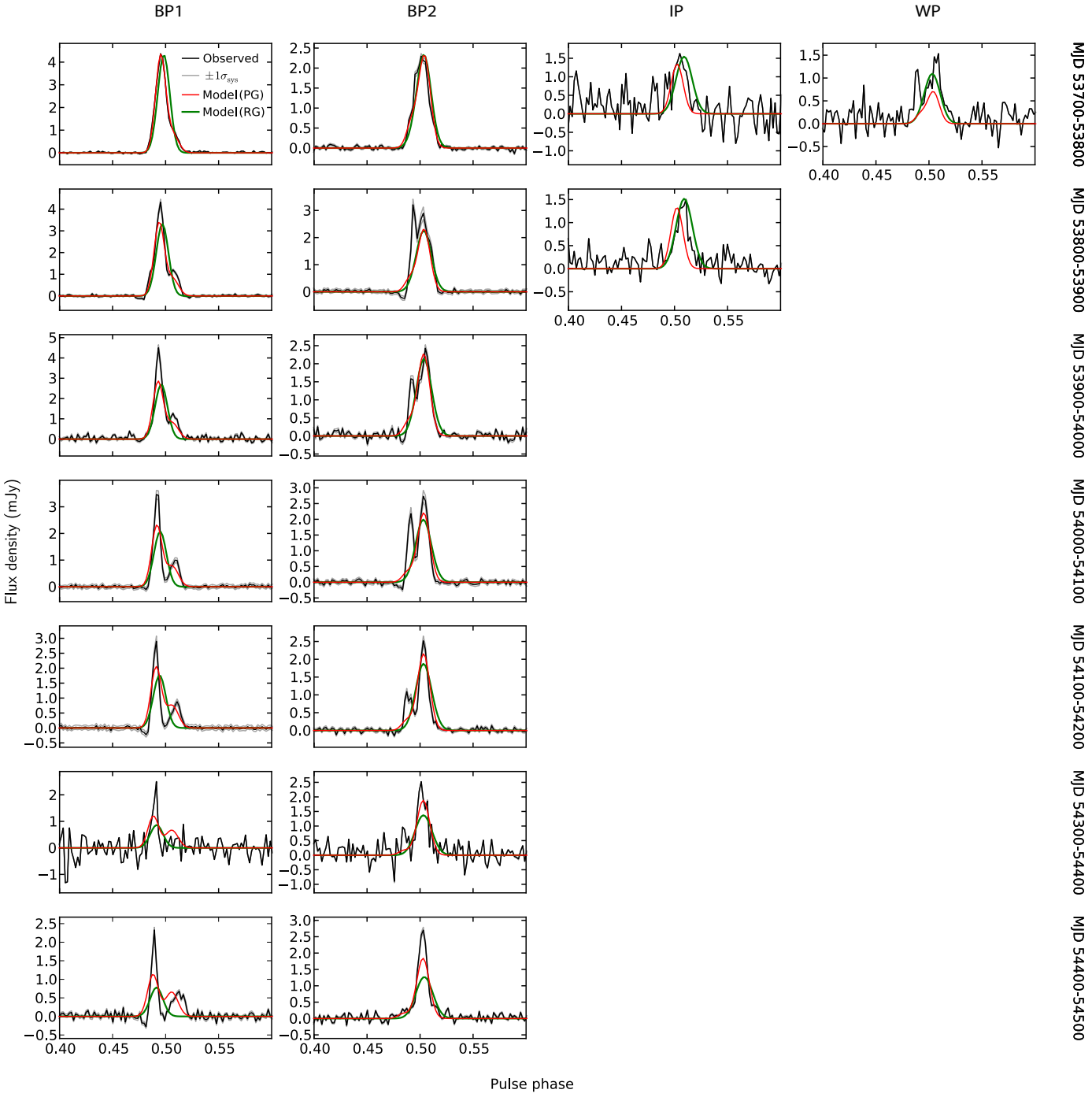

Fig. B.4. continued.

Appendix C: 3D geometry

The following figures accompany the description of our model's geometry, presented in Sect. 4.2, as well as the description of the most likely beam shape of pulsar B, presented in Sect. 4.5.

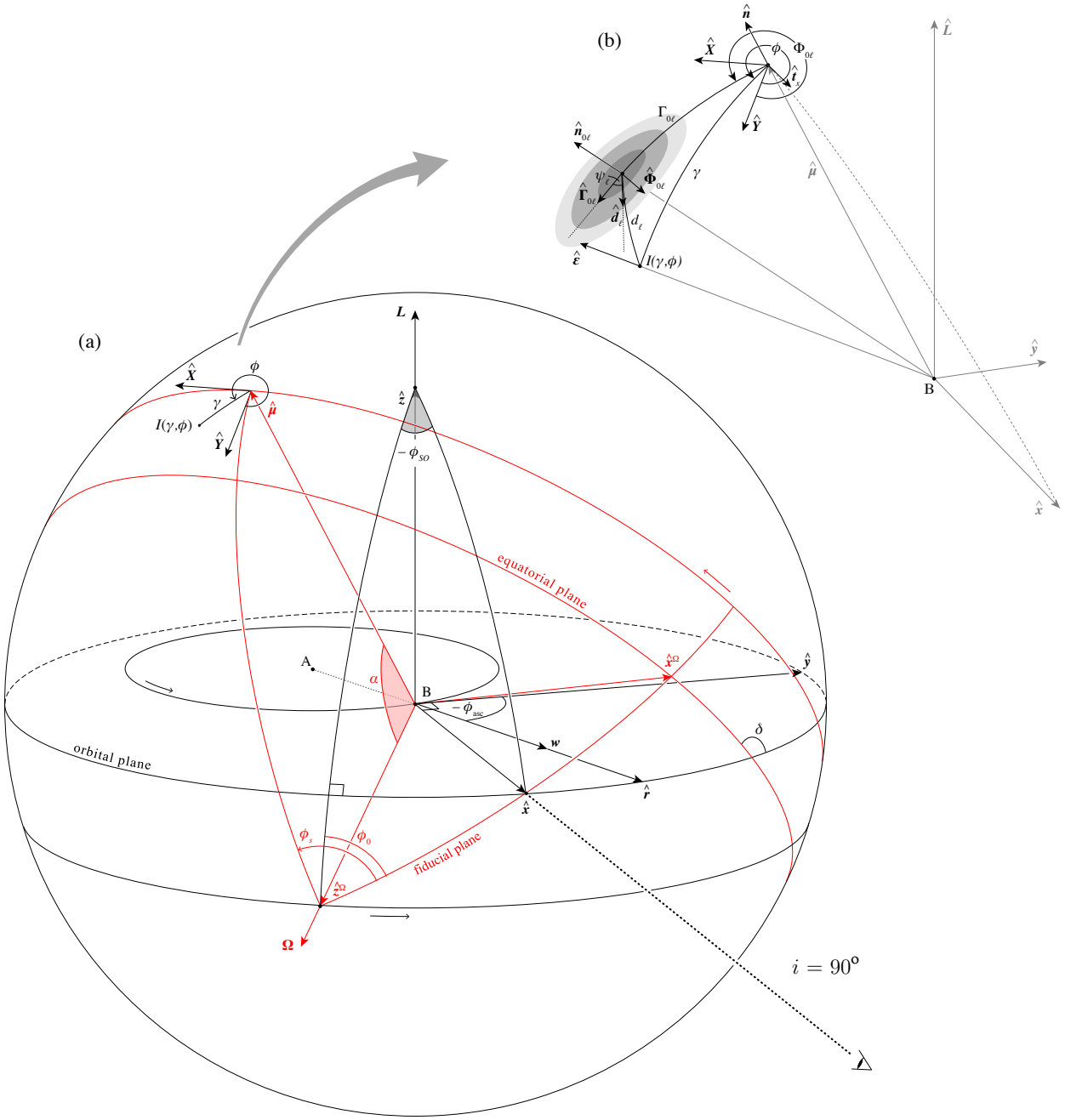

Fig. C.1. (*a*) Geometry of the model used in this work to describe the effect of the radial wind of pulsar A ($\boldsymbol{w}$) on the emission of pulsar B. In this figure, $\boldsymbol{\Omega}$ and $\hat{\boldsymbol{\mu}}$ are the spin and magnetic moment of pulsar B, respectively, and $\boldsymbol{L}$ is the orbital angular momentum of the binary system. For clarity, we separated the elements corresponding to the frame of the orbit ($\{\hat{\boldsymbol{x}}, \hat{\boldsymbol{y}}, \hat{\boldsymbol{z}}\}$) and those corresponding to the frame of the pulsar ($\{\hat{\boldsymbol{x}}^{\Omega}, \hat{\boldsymbol{y}}^{\Omega}, \hat{\boldsymbol{z}}^{\Omega}\}$) in black and red, respectively. The sense of pulsar B's orbit around pulsar A and that of $\boldsymbol{\mu}$ about $\boldsymbol{\Omega}$ are shown with black and red arrows, respectively. Also shown with a black arrow is the sense of the geodetic precession of $\boldsymbol{\Omega}$ about $\boldsymbol{L}$ (defined by an increasing $\phi_{\rm SO}$). We note that, compared to Breton et al. (2008), we used the opposite direction for $\boldsymbol{L}$. The direction to the observer coincides with the unit vector $\hat{\boldsymbol{x}}$. In this work, we have assumed that the double pulsar system is viewed exactly edge-on: so, the orbital inclination, i, is exactly equal to 90°. At the position of $\hat{\boldsymbol{\mu}}$, we show an example location in the beam, with beam coordinates (γ, ϕ), corresponding to intensity $I(\gamma, \phi)$ (see Eq. (10)). For the definition of the reference frames and angles shown, the reader is directed to Sect. 4.2. (*b*) The definitions of the angles that are used in our parametrisation of pulsar B's emission beam location and intensity.

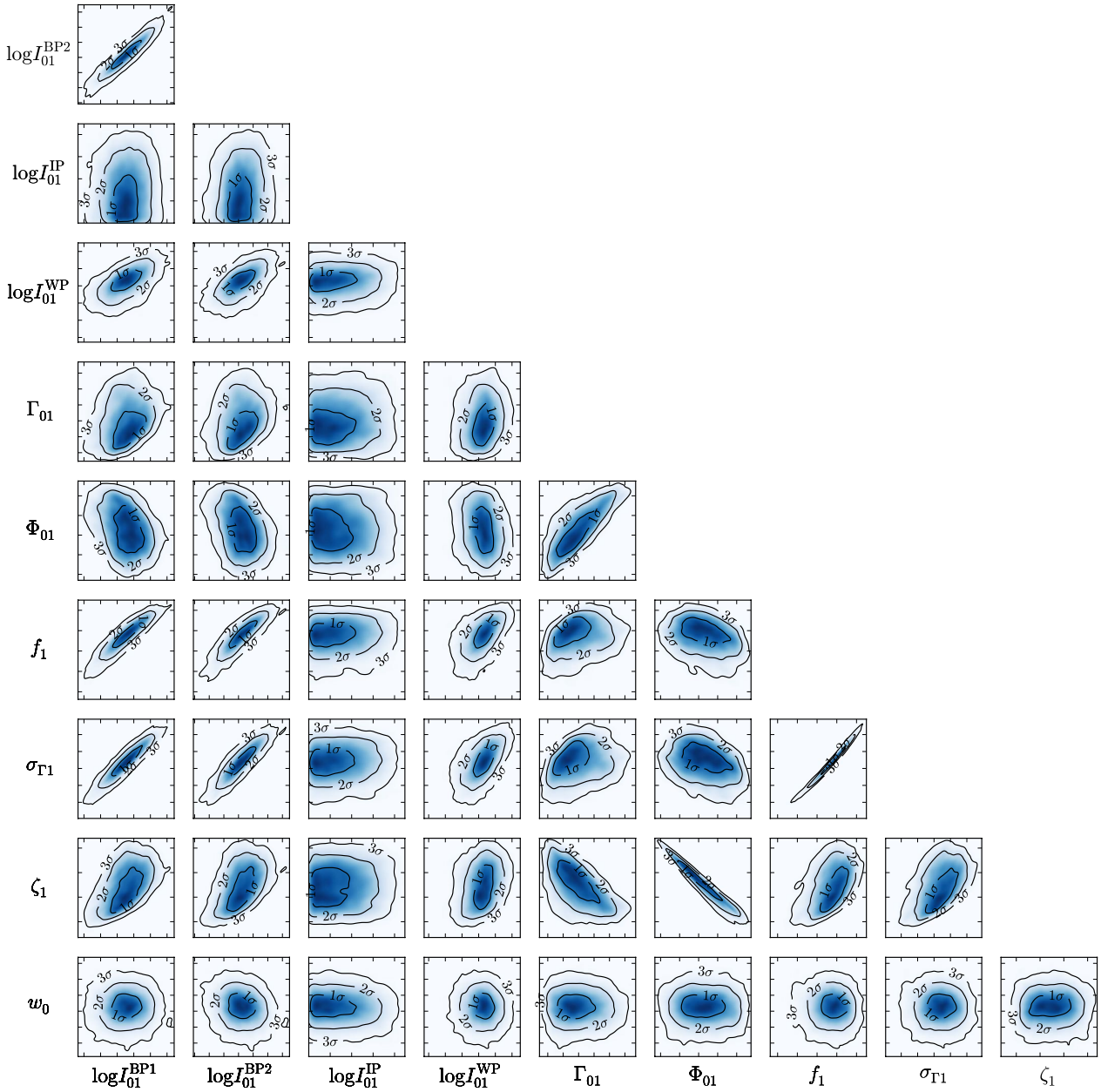

Fig. C.2. Matrix of probability density plots between the model parameters corresponding to the first Gaussian component in our beam model (indexed with "01" in Table 3), plus the wind magnitude.

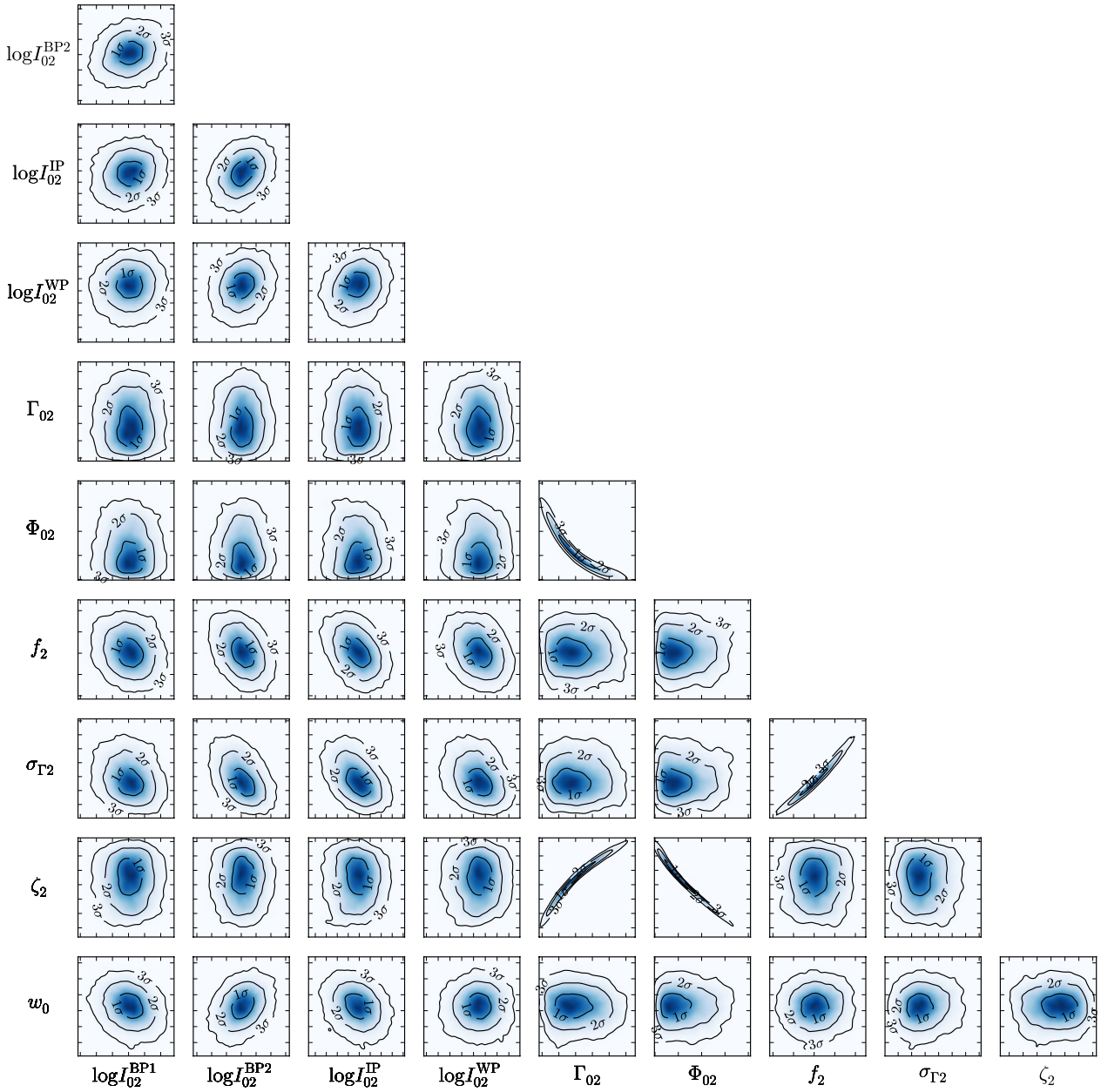

Fig. C.3. Same as in Fig. C.2, for the second Gaussian component in our beam model (indexed with "02" in Table 3).